

1 **On the remote impacts of mid-Holocene Saharan vegetation on South**
2 **American hydroclimate: a modelling intercomparison**

3
4 **S. Tiwari¹, R. D. Ramos², F. S. R. Pausata¹, A. N. LeGrande^{3,4}, M. L. Griffiths², H. Beltrami⁵,**
5 **I. Wainer⁶, A. de Vernal¹, D. T. Litchmore^{4,3}, D. Chandan⁷, W. R. Peltier⁷, and C. R. Tabor⁸**

6
7 ¹Centre ESCER (Étude et la Simulation du Climat à l'Échelle Régionale) and GEOTOP (Research
8 Center on the dynamics of the Earth System), Department of Earth and Atmospheric Sciences,
9 University of Quebec in Montreal, Montreal, Canada.

10 ²Department of Environmental Science, William Paterson University, Wayne, New Jersey, USA.

11 ³NASA Goddard Institute for Space Studies, New York, New York, USA.

12 ⁴Center for Climate Systems Research, Columbia University, New York, New York, USA.

13 ⁵Department of Earth Sciences, St. Francis Xavier University, Antigonish, Nova Scotia, Canada.

14 ⁶Departamento de Oceanografia Física, Química e Geológica, Instituto Oceanográfico da
15 Universidade de São Paulo, Praça do Oceanográfico, Sao Paulo, Brazil.

16 ⁷Department of Physics, University of Toronto, Toronto, Ontario, Canada.

17 ⁸Department of Geosciences, University of Connecticut, Storrs, Connecticut, USA.

18
19 Corresponding author: Shivangi Tiwari (tiwari.shivangi@courrier.uqam.ca)

20
21 **Key Points:**

- 22 • We simulate the mid-Holocene with and without the Green Sahara using four fully coupled
23 global climate models
- 24 • The mid-Holocene simulation with the Green Sahara shows intensification of orbitally-
25 driven changes in precipitation over northern Africa and South America
- 26 • Incorporation of the Green Sahara leads to greater proxy-model agreement over both
27 northern Africa and South America
- 28

29 **Abstract**

30 Proxy reconstructions from the mid-Holocene (MH: 6,000 years ago) indicate an intensification
31 of the West African Monsoon and a weakening of the South American Monsoon, primarily
32 resulting from orbitally-driven insolation changes. However, model studies that account for MH
33 orbital configurations and greenhouse gas concentrations can only partially reproduce these
34 changes. Most model studies do not account for the remarkable vegetation changes that occurred
35 during the MH, in particular over the Sahara, precluding realistic simulations of the period. Here,
36 we study precipitation changes over northern Africa and South America using four fully coupled
37 global climate models by accounting for the Saharan greening. Incorporating the Green Sahara
38 amplifies orbitally-driven changes over both regions, and leads to an improvement in proxy-
39 model agreement. Our work highlights the local and remote impacts of vegetation and the
40 importance of considering vegetation changes in the Sahara when studying and modelling global
41 climate.

42 **Plain Language Summary**

43 Paleoclimate modelling offers a way to test the ability of climate models to detect climate change
44 outside the envelope of historical climatic variability. The mid-Holocene (MH: 6,000 years ago)
45 is a key interval for paleoclimate studies, as the Northern Hemisphere received greater summer-
46 time insolation and experienced stronger monsoons than today. Due to a stronger MH West
47 African Monsoon, the Saharan region received enough rainfall to be able to host vegetation. The
48 vegetation changes in the Sahara affected not only the local climate but also far-afield locations
49 through teleconnections in the global climate system. In this study, we simulate the MH climate
50 using four climate models, each with two types of simulations – with and without the Green Sahara.
51 We show that simulations with the Green Sahara capture greater drying over the South American
52 continent than the simulations which only account for changes in orbital forcing and greenhouse
53 gas concentrations. The simulations with the Green Sahara are more in line with proxy
54 reconstructions, lending further support to incorporating vegetation changes as a necessary
55 boundary condition to simulate the MH climate realistically.

56 **1 Introduction**

57
58 Vegetation cover is known to impact regional climate variability, but the magnitude and global
59 implications of vegetation changes are not well constrained due to the limited variability over the
60 historical period. The Paleoclimate Modelling Intercomparison Project (PMIP) coordinates
61 experiments to determine consistent responses across models that, when constrained against
62 proxy reconstructions, can provide for a deeper understanding of how the climate system
63 operates (Braconnot et al., 2012; Otto-Bliesner et al., 2017; Kageyama et al., 2018). A key
64 interval for study is the mid-Holocene (MH), which refers to the time-slice around 6,000 years
65 ago. The MH was characterized by paleogeographic and ice-sheet distributions comparable to
66 today, but the orbital configuration and greenhouse gas (GHG) composition differed. Most
67 notably, the perihelion occurred during boreal autumn as opposed to boreal winter today,
68 enhancing Northern Hemisphere seasonality. The Northern (Southern) Hemisphere received
69 greater (lesser) summer insolation relative to the present day. In addition, carbon dioxide and
70 methane compositions were lower by ~7% and ~26% respectively, relative to the pre-industrial
71 (PI) period (Otto-Bliesner et al., 2017). These differences are prescribed in the coordinated
72 PMIP4 *midHolocene* experiments. The PMIP4 MH simulations indicate stronger monsoons in

73 the Northern Hemisphere, especially over northern Africa (Brierley et al., 2020). This is
74 supported by multi-proxy reconstructions from various archives such as organic biomarkers
75 (Shanahan et al., 2015; Collins et al., 2017; Tierney et al., 2017), dust (McGee et al., 2013;
76 Palchan et al., 2019), pollen (Bartlein et al., 2011; Hély et al., 2014), speleothems (Sha et al.,
77 2019) and paleohydrological records (Gasse et al., 2000; Lézine et al., 2011). However, proxy-
78 model comparisons indicate that climate models generally under-estimate the magnitude of
79 African precipitation change with too little rainfall to support the proxy reconstructed vegetation
80 (Braconnot et al., 2012; Tierney et al., 2017; Brierley et al., 2020).

81
82 The proxy-model discrepancy over northern Africa may be resolved to great extent through the
83 incorporation of appropriate vegetation in climate models. There is considerable evidence that
84 there were large-scale vegetation changes throughout the world during the MH (Bartlein et al.,
85 2011). Most notably, the expansion of grasslands and shrubs into the current desert region of the
86 Sahara (the so-called “Green Sahara”; e.g., Hély et al., 2014) led to significant amplification of
87 the orbital-driven strengthening of the West African Monsoon (WAM) through positive non-
88 linear feedbacks such as vegetation, dust and albedo feedbacks (Swann et al., 2014; Pausata et
89 al., 2020). The incorporation of these changes, either through dynamic vegetation (e.g., Levis et
90 al., 2004; Rachmayani et al. 2015; Dallmeyer et al., 2021) or through the prescription of
91 vegetation distributions (e.g., Pausata et al., 2016; Chandan and Peltier, 2020, Thompson et al.,
92 2021), leads to simulations that are more consistent with proxy reconstructions. An important
93 consequence of more realistic simulations is the enhanced ability to identify the far-afield
94 impacts of the Green Sahara. For example, simulations accounting for the MH Green Sahara
95 have elucidated the influence of the WAM on the El-Niño Southern Oscillation (Pausata et al.,
96 2017a), tropical cyclone activity (Pausata et al., 2017b), global monsoon systems (Sun et al.,
97 2019; Griffiths et al., 2020; Piao et al., 2020; Tabor et al., 2020, Huo et al., 2021) and high
98 latitude climate (Muschitiello et al., 2015). While the regional changes that accompanied the
99 Green Sahara are well-recognized, its remote impacts warrant further exploration.

100
101 The MH WAM intensification occurred in parallel with a reduction in precipitation over parts of
102 South America. Proxy reconstructions from pollen, sedimentological and isotopic records
103 indicate that a drier MH climate prevailed over most of tropical South America (Baker et al.,
104 2001; Cruz et al., 2005; Novello et al., 2017; see Gorenstein et al., 2022 for a synthesis); some
105 exceptions are found from the Cariaco Basin (Haug et al., 2001), northeast Brazil (Cruz et al.,
106 2009) and western Amazonia (Wang et al., 2017). While PMIP4 models in general capture this
107 reduction in precipitation (Brierley and Wainer, 2018; Brierley et al., 2020), closer inspection
108 reveals less consistency amongst them regarding the reduction in South American precipitation,
109 compared with northern Africa where the models display better agreement (Brierley et al., 2020).

110
111 The South American Monsoon System (SAMS) brings precipitation during austral summer over
112 the region extending from southern Amazon to southeastern Brazil (Garreaud et al., 2009). The
113 MH drying over South America has been attributed primarily to lower summer insolation and
114 dampened seasonality in the Southern Hemisphere, which led to a weakening of the SAMS.
115 However, few studies have addressed the mechanisms by which the Green Sahara could have
116 impacted South American climate. Dias et al. (2009) studied the effect of vegetation changes
117 with two MH experiments: the first considered changes only in orbital parameters, the second
118 additionally incorporated vegetation changes by asynchronously coupling a vegetation model to

119 an ocean-atmosphere climate model. They observed that vegetation feedbacks could enhance
120 some orbitally driven patterns, especially the displacement of the Intertropical Convergence
121 Zone (ITCZ). Recently, Tabor et al. (2020) used a water isotope-enabled Earth System Model to
122 simulate $d^{18}O$ changes during the MH and compare them with speleothem reconstructions. They
123 found that the incorporation of the Green Sahara led to better proxy-model agreement with the
124 amplification of the drying signal over South America.

125
126 Therefore, tropical African vegetation changes are a critical prerequisite for a realistic simulation
127 of MH climate, as well as for the identification of the remote impacts of the Green Sahara. In this
128 study, we investigate the response of the climate of northern African and South America to the
129 incorporation of a Green Sahara. To this end, we examine the differences between two MH
130 simulations – with and without the Green Sahara – based on simulations from four coupled
131 global climate models. To the best of our knowledge, this is the first model intercomparison
132 study regarding the effects of land surface changes due to the Green Sahara. We also present a
133 semi-quantitative assessment of the improved proxy-model agreement upon the inclusion of the
134 Green Sahara, which lends further support to our approach.

135 136 137 **2 Methods**

138 139 **2.1 Climate models and experiments**

140 For this study, we analyzed outputs from four global climate models – (i) EC-Earth version 3.1
141 (Hazeleger et al., 2010), (ii) the water isotope-enabled Community Earth System Model version
142 1.2 (iCESM1; Brady et al., 2019), (iii) University of Toronto version of CCSM4 (hereby referred
143 to as UofT-CCSM4; Peltier and Vettoretti, 2014) and (iv) the water isotope-enabled GISS-E2.1-
144 G (Kelley et al., 2020). Details about the atmospheric and oceanic components of these models
145 and their associated grids are provided in Table S1. Three simulations were analyzed for each
146 model – one for the pre-industrial (PI) and two for the mid-Holocene (MH) climate state. The
147 first MH experiment follows the standard forcings and boundary conditions as specified by the
148 PMIP4 guidelines (Otto-Bliesner et al., 2017) and is referred to as MH_{PMIP} . These guidelines
149 comprise changes to orbital parameters and greenhouse gas concentrations. The second MH
150 simulation, which additionally incorporates a Green Sahara by prescribing vegetation over
151 northern Africa, is referred to as the MH_{GS} . While the representation of the Green Sahara is
152 different in each climate model, it broadly follows the paleodistributions of vegetation suggested
153 for the PMIP4 sensitivity experiments (Otto-Bliesner et al., 2017). The vegetation change leads
154 to a reduction in surface albedo from ~ 0.3 to 0.15-0.19 over the Sahara. Further details about the
155 representation of the Green Sahara in the MH_{GS} experiment in the different models is provided in
156 the Supplementary Text S1.

157
158 To validate the models, we compared climatological outputs from PI simulations with the Global
159 Precipitation Climatology Centre (GPCC) Reanalysis Dataset from 1951-80 (Schneider et al.,
160 2011) and the Global Precipitation Climatology Project (GPCP) dataset v2.2 from 1979-2009
161 (Huffman et al., 2015) (Text S1 and Fig. S2). The models broadly reproduce the magnitudes and
162 distributions of annual precipitation over the study area. iCESM 1.2 shows a dry bias over
163 northwestern South America (~ 2 mm/day). Notwithstanding some local precipitation hotspots,
164 GISS-E2.1-G shows a dry bias over the domain of the SAMS (which extends from southern

165 Amazon to southeastern Brazil), as well as over the Sahel. To redress the effect of model biases,
 166 we discuss our results in terms of MH – PI differences. Only differences significant at the 95%
 167 confidence level are shown. We interpret the MH_{PMIP} - PI anomalies to reflect the effects of
 168 changes in orbital parameters and greenhouse gas concentrations, and the MH_{GS} - MH_{PMIP}
 169 anomalies to reflect the additional effect of the Green Sahara. All model climate variables are
 170 analyzed as averages over 100 simulation years.

171

172 **2.2 Precipitation proxies**

173 To compare the effects of the Green Sahara on monsoon regimes within northern Africa and
 174 South America, we considered precipitation proxies from terrestrial and marine records within
 175 these respective domains: 0° - 38° N; 20° W- 45° E and 50° S- 15° N; 80° W- 30° W. The proxy data,
 176 derived from previously synthesized databases, includes records of pollen-based mean annual
 177 precipitation reconstructions (Bartlein *et al.*, 2011), lake level records from Africa (Tierney *et al.*
 178 *et al.*, 2011), and an updated multiproxy hydroclimate reconstruction from South America
 179 (Gorenstein *et al.*, 2022). We also included hydroclimate reconstructions from Bolivia, Colombia
 180 and Peru (Harrison *et al.*, 2003) to fill in more data gaps in the tropical South American region.
 181 In total, we have collated 252 proxy records in which each MH hydroclimate response relative to
 182 PI is compared against model outputs.

183

184 **2.3 Proxy-model comparison**

185 To compare the proxies with models, MH precipitation responses relative to PI conditions were
 186 all categorically defined as either drier (rated as -1), wetter (1), or unchanged (0). Field
 187 reconstructions of mean annual precipitation from (Bartlein *et al.*, 2011) were converted to these
 188 categories based on the reported change for each grid point. Original classifications of lake level
 189 reconstructions from Africa (i.e., “low”, “intermediate”, and “high” (Tierney *et al.*, 2011)) for
 190 MH and PI periods were used to derive lake level status. These included higher, lower and
 191 unchanged to represent wetter, drier and unchanged, respectively. Categories for hydroclimate
 192 reconstructions from South America and additional records in this region follow the
 193 interpretation of the original publications (i.e., Harrison *et al.*, 2003; Gorenstein *et al.*, 2022).
 194 Simulated changes in precipitation from the nearest grid points to the proxy sites were extracted
 195 and similarly placed into three categories based on the direction of change and statistical
 196 significance.

197

198 To quantify the agreement between models and proxies, we used Cohen’s κ statistic defined as
 199 the observed fractional agreement (p_o) between raters (i.e., proxies and models) relative to the
 200 probability of random agreement (p_e):

$$201 \quad \kappa = \frac{p_o - p_e}{1 - p_e};$$

202 where p_o is the sum of the diagonal elements in the proxy-model matrix divided by the total
 203 number of samples, N ; and p_e is the product of the sum of each matrix row and column (given by
 204 the frequency of occurrence of each category) normalized by N . We implemented weights in the
 205 κ calculation by multiplying the data by a weight matrix that penalizes models for a total
 206 disagreement (i.e., drier when it should be wetter and vice versa) to a value of 0 and near miss
 207 (i.e., drier or wetter when it should be unchanged) to a value of 0.5.

208

209

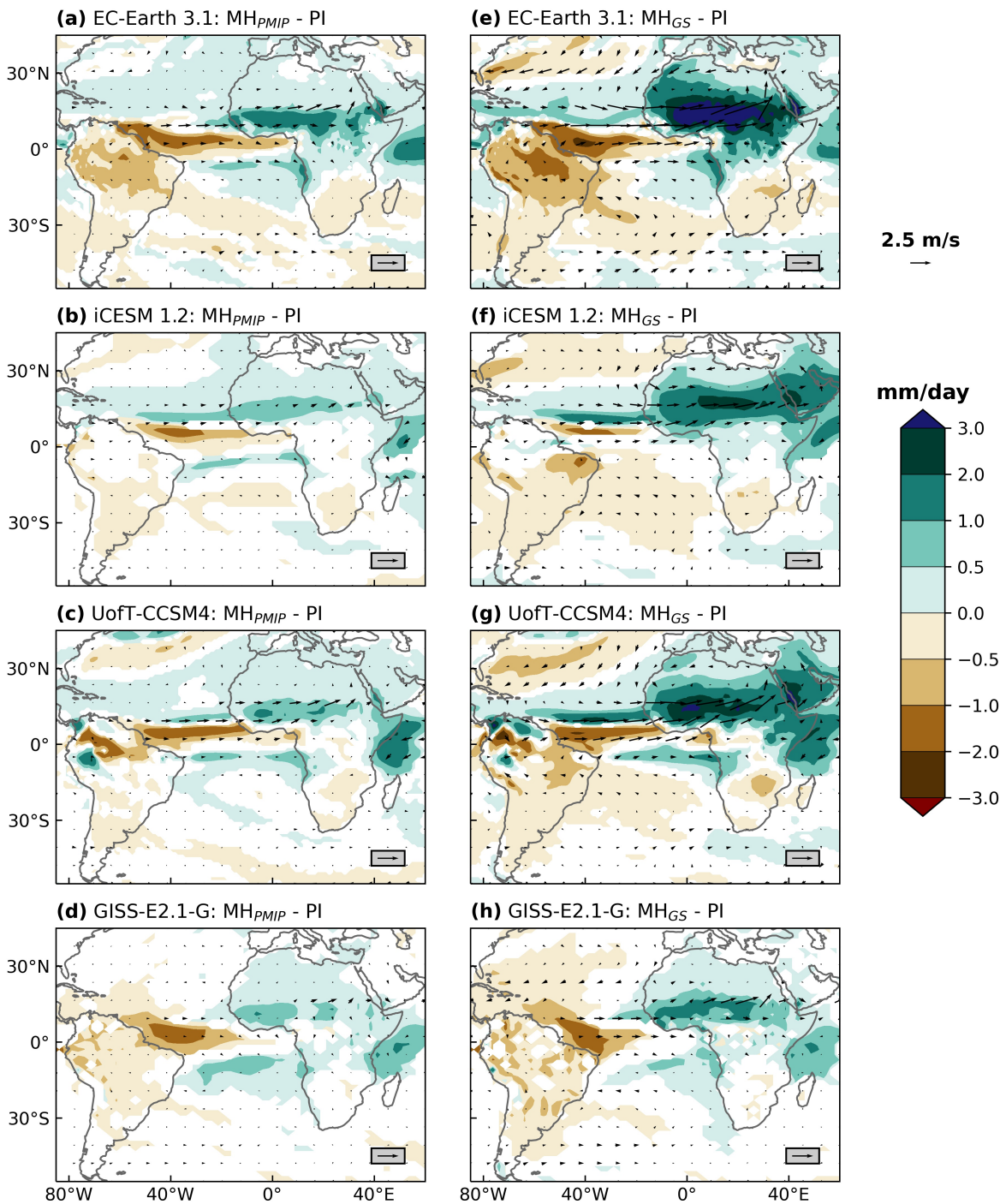
3 Results

210
211
212 The MH_{PMIP} simulations indicate a small but significant increase in precipitation of 0.5 mm/day
213 over almost the entirety of northern Africa, extending beyond 30 °N (Fig. 1, a-d). The
214 intensification of the WAM is larger over the Sahel, where it reaches the order of 1-2 mm/day
215 between the equator and 15 °N and is also reflected in stronger low-level (850 hPa)
216 southwesterly monsoon winds. An increase of 0.5 mm/day and 2 mm/day is consistent with the
217 northward expansion of Sahelian and Sudanian vegetation into the Sahara and the Sahel
218 respectively, as indicated by pollen records (Hély et al., 2014). The patterns and magnitude of
219 the increase in mean annual precipitation over northern Africa are consistent across all four
220 models. EC-Earth 3.1 shows the highest increase of 2 mm/day over the core rainfall belt. The
221 intensification of the WAM in the MH_{PMIP} simulations is accompanied by a decrease in mean
222 annual precipitation over some regions of South America. This decrease is on the order of 0.5-2
223 mm/day but the spatial extent of the change differs among the models. EC-Earth 3.1 and GISS-
224 E2.1-G capture a widespread decrease across nearly the full meridional extent of the continent.
225 The UofT-CCSM4 simulation shows a greater decrease, but limited to parts of northwestern
226 Amazon, while iCESM 1.2 shows a modest decrease of up to 0.5 mm/day in the southern half of
227 the continent. All models show a decrease in precipitation just north of the equator in the
228 Atlantic Ocean.

229
230 Comparing the MH_{PMIP} (Fig. 1, a-d) and the MH_{GS} (Fig. 1, e-h) simulations, we observe an
231 amplification of orbitally-driven changes in rainfall. The increase in precipitation over northern
232 Africa is intensified and extends further north, with three out of four models showing an increase
233 of 0.5-1 mm/day up to 25 °N. The core rainfall belt is between 10-20 °N, with an increase in
234 precipitation in the order of 1-3 mm/day. EC-Earth 3.1 shows the greatest increase in the core
235 rainfall belt, exceeding 4 mm/day between 12-16 °N. This is consistent with the northward
236 expansion of tropical Guineo-Congolian vegetation, in addition to the changes in Sahelian and
237 Sudanian vegetation extents (Hély et al., 2014). Across the Atlantic, all models suggest greater
238 and more widespread drying of up to 2 mm/day over South America. The drying patterns appear
239 stronger over northern South America, but more consistent over southern South America.
240 Notably, iCESM 1.2 shows little change from the PI over northwestern South America, with a
241 modest but significant increase in some parts of the Amazon. All models show a decrease in
242 precipitation immediately north of the equator and an intensification in precipitation northwards
243 of this region, suggesting a northward shift in the position of the ITCZ. None of the MH
244 simulations indicate an increase in precipitation over northeastern Brazil.

245

246



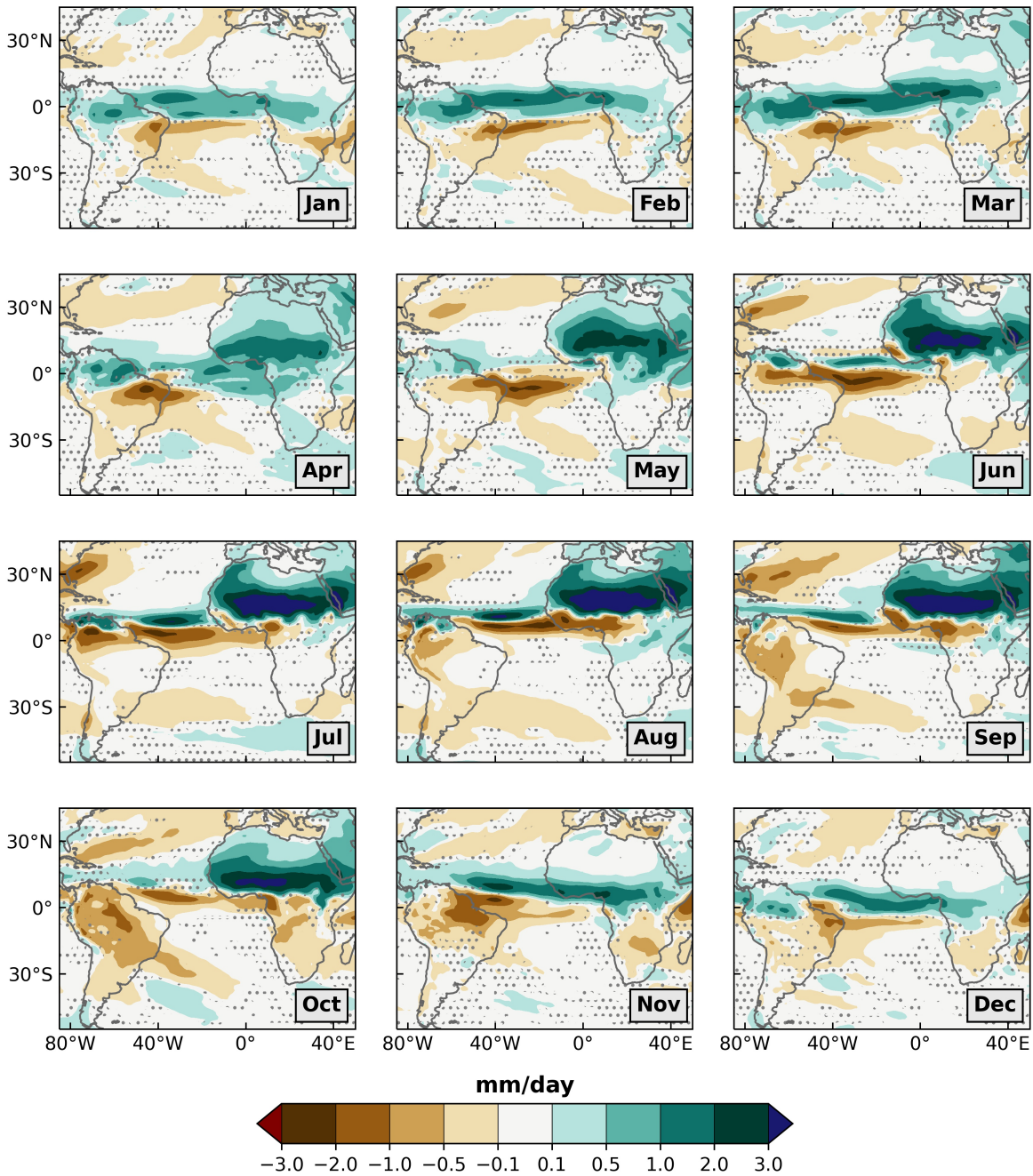
247
 248 **Figure 1. Change in annual precipitation in the MH_{PMIP} (a-d) and MH_{GS} (e-f) experiment**
 249 **relative to the PI simulation. Colors represent precipitation change in mm/day. Only**
 250 **changes significant at the 95% confidence level are shaded. Vectors indicate changes in**
 251 **low-level (850 hPa) wind strength.**
 252
 253

254 As the WAM and the SAMS operate over different seasons and different regions in South
255 America experience different annual precipitation cycles (Fig. S1), it is helpful to investigate
256 MH-PI anomalies in monthly precipitation. The multi-model mean rainfall changes in the
257 MH_{PMIP} simulation relative to the PI indicate an intensification of the WAM from May-October
258 (Fig. S3). With the exception of austral spring (October-November), the dominant change
259 observed over South America is a drying throughout the year. During austral winter (May-July),
260 this drying is restricted to regions north of 10 °S, which are dominantly influenced by the ITCZ.
261 The multi-model mean change in the MH_{GS} relative to PI indicate that the increase in
262 precipitation over northern Africa lasted longer, from March-November, with a very prominent
263 increase over the core rainfall belt around 15 °N from May-October (Fig. S4). Two notable
264 patterns are observed in the MH_{GS} simulation relative to the PI: firstly, except for November, the
265 domain of the SAMS was drier throughout the year; secondly, the ITCZ-influenced regions in
266 northern South America were wetter between January-May and drier through the rest of the year.
267 Changes in annual average values aggregate some of these seasonal changes and result in a
268 weaker drying signal in the MH_{PMIP} simulation relative to the PI. However, since the drying
269 signal is stronger, more widespread, and extended to a longer duration through the year in the
270 MH_{GS} simulation relative to the PI, it remains evident in the annual average as well (Fig. 1).

271
272 The effects of incorporating the Sahara greening into the models are evident in the multi-model
273 mean anomalies between MH_{GS} and MH_{PMIP} (Fig. 2). The Sahara greening leads to higher
274 precipitation over northern South America between December-May, but drying over other
275 regions throughout the year. Notably, the Green Sahara leads to a larger amplitude of
276 precipitation seasonality in the equatorial areas such as the northern Amazon. This is because the
277 expansion of the seasonal migration range of the ITCZ in the MH_{GS} scenario leads to an increase
278 in precipitation over equatorial South America during austral summer and a decrease during the
279 boreal summer. Lastly, the Saharan vegetation changes are associated with drying over
280 northeastern Brazil throughout the year.

281

282

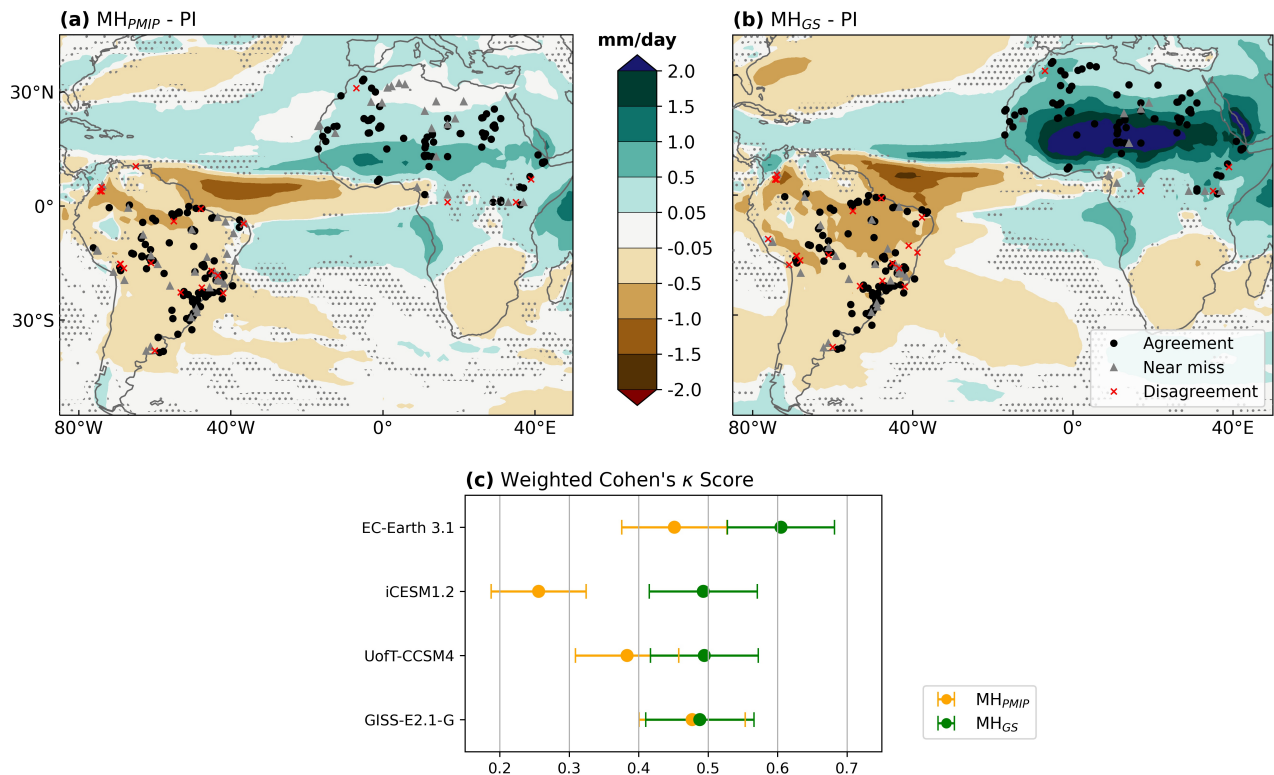


283
284
285
286
287
288
289

Figure 2. Monthly evolution of the multi-model average precipitation anomalies between MH_{GS} and MH_{PMIP} . Areas in which less than three models agree on the sign change are hatched.

290 We assessed the agreement between proxies and models under different MH experiments using
291 weighted Cohen's κ statistic, a semi-quantitative metric to estimate the frequency of agreement
292 between categorical data. All models show higher κ scores in the MH_{GS} (i.e., $\kappa > 0.49$, $p < 0.01$)
293 compared to MH_{PMIP} (i.e., $\kappa < 0.48$, $p < 0.01$) experiment, with EC-Earth 3.1 and iCESM 1.2

294 showing the most significant improvements (Fig. 3; Fig. S5a; Fig. S6). This indicates that the
 295 MH_{GS} simulation better simulates the extent of a wetter northern Africa and/or a drier South
 296 America during this period relative to the MH_{PMIP} simulation. Considering the proxy-model
 297 agreement between the continents, northern Africa consistently shows higher κ scores than South
 298 America (Fig. S5b and S5c) with all models showing a general improvement in reflecting a
 299 greener Sahara. Over South America, all models except for GISS-E2.1-G show an improvement
 300 in capturing the drier conditions in this region in the MH_{GS} experiment (Fig. S5c). UofT-CCSM4
 301 performed well over northern Africa but worse over South America resulting in overall
 302 comparable κ scores between MH scenarios (Fig. 3; Fig. S5). For GISS-E2.1-G, the κ score over
 303 South America decreases but there is a general improvement over northern Africa in the MH_{GS}
 304 simulation with comparable κ scores between MH experiments (Fig. 3; Fig. S5). The observed
 305 overall improvement in iCESM 1.2 originates from the more apparent drying over South
 306 America under MH_{GS} relative to MH_{PMIP} (Fig. 1). EC-Earth 3.1 shows the highest κ score for
 307 both continents, outperforming all models under MH_{GS} scenarios (Fig. S5).
 308
 309



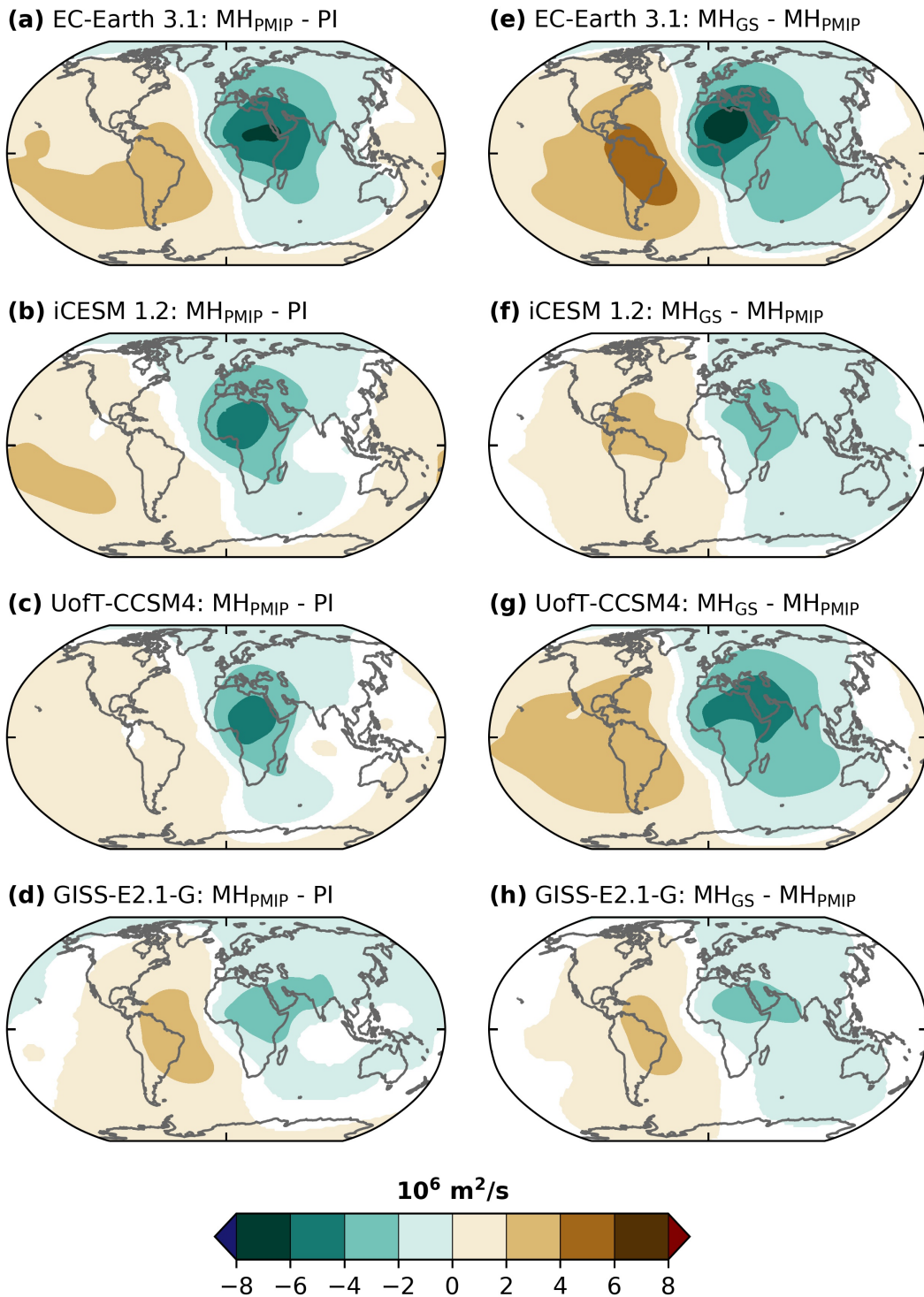
310
 311 **Figure 3. Multi-model mean change in annual precipitation, with proxy-model agreement**
 312 **overlayed. Colors indicate (a) MH_{PMIP} – PI and (b) MH_{GS} – PI changes in annual**
 313 **precipitation in mm/day. Areas in which less than three models agree on the sign change**
 314 **are hatched. Proxy-model agreement is indicated as agreement (black circles), near miss**
 315 **(grey triangles) or disagreement (red crosses). (c) Weighted Cohen’s κ Scores for MH_{PMIP}**
 316 **(orange symbols) and MH_{GS} (green symbols) runs. Error bars indicate 95% confidence**
 317 **intervals.**

318
 319

4 Discussion and Conclusions

In this study, we studied the impact of paleovegetation changes during the MH by considering two simulations – with and without the Green Sahara. A model intercomparison to robustly assess the northern African land cover changes was hitherto missing. For the first time, we compare four different Earth system models in which vegetation changes over northern Africa are account for, and focus on the associated hydroclimate changes over northern Africa and South America. Irrespective of the methods used to prescribe vegetation, the models share similarities in their teleconnections across the tropical and extra-tropical Atlantic. Thus, while different models include different aspects of the Green Sahara-modulated climate impact through varying vegetation, dust, soil and lake modifications, they show similar responses, owing to the overwhelming importance of these vegetation changes. The Sahara greening (MH_{GS}) enhances the rainfall over northern Africa, while further decreasing precipitation over South America relative to the case in which only orbital forcing are accounted for (MH_{PMIP}).

Several modelling studies have shown a reduction in precipitation over South America as well as changes to the monsoonal cycle due to changes in seasonal insolation (Shimizu et al., 2021). The orbital-driven weakening of the SAMS during austral summer is indicated by PMIP3 (Prado et al., 2013, Shimizu et al., 2020) as well as PMIP4 models (Brierley et al., 2020). Our MH_{PMIP} simulations similarly capture a drying signal, particularly over northwestern South America (Fig. 1) and provide drying estimates comparable to previous results (around 1 mm/day). Examining the seasonal cycle indicates that South America received less insolation during austral summer and more insolation during austral spring during the mid-Holocene compared with the PI, which could have altered the cycle of the SAM (Shimizu et al., 2020). Our MH_{PMIP} simulations also capture these changes through a decrease in precipitation over the SAMS region during December-February, but an increase during October-November. However, few of the previous modelling studies focused specifically on how the Sahara greening may have influenced the MH South American hydroclimate (Dias et al., 2009; Tabor et al., 2020). Our results support their findings regarding the impact of the Green Sahara in amplifying orbital-driven weakening of the SAMS, through consistent results from four different models. Furthermore, in our study we show that South America also experienced a significant reduction in precipitation during austral winter, most likely because the prescribed vegetation led to widespread moisture redistribution during austral winter (Fig. 2). Combined with a weakening of the SAMS during austral summer, this led to longer and greater drying over South America than seen when only considering changes in orbital forcings. Thus, the drying in South America during the MH was prevalent throughout the year and not exclusively related to changes in the SAMS.



360
361
362
363
364
365

Figure 4. Changes in boreal summer (JJAS) upper-level (200 hPa) velocity potential (a-d) for the MH_{PMIP} relative to the PI experiment and (e-h) for the MH_{GS} relative to the MH_{PMIP} simulation. Only changes significant at the 95% confidence level are shaded.

366
367 Various mechanisms have been proposed to explain the influence of northern African vegetation
368 changes on South American hydroclimate. Dias et al. (2009) suggested a northward migration of
369 the SACZ associated with a weakening of the upper-level Bolivian High and a weakened tropical
370 circulation. Tabor et al. (2020) discussed the role of substantial regional warming due to a Green
371 Sahara, which acted to counteract the effects of increased insolation in the Southern Hemisphere
372 in pulling the ITCZ southwards between November and March. The precipitation over South
373 America was likely also modulated by changes in the equatorial Atlantic (Brierley and Wainer,
374 2018) and the equatorial Pacific variability (Pausata et al., 2017). While an in-depth investigation
375 of the mechanism(s) behind the Green Sahara's modulation of South American hydroclimate is
376 beyond the scope of this study, our work nonetheless shows the importance of Saharan
377 vegetation in more accurately simulating northern African and South American teleconnections
378 during the MH. This is even clearer through an analysis of boreal summer (JJAS) atmospheric
379 circulation, namely upper-level (200 hPa) velocity potential (Fig. 4). A comparison of $MH_{PMIP} -$
380 PI and $MH_{GS} - MH_{PMIP}$ anomalies shows that the impact of the Green Sahara is comparable to
381 the impact of the changes in orbital configuration and GHG concentrations (Fig. 4). An
382 inadequate representation of the substantial forcing imposed by the Saharan vegetation precludes
383 an analysis of its remote impacts.

384
385 The inclusion of vegetation changes over northern Africa in the models (MH_{GS} experiments) also
386 leads to an overall improvement in proxy-model agreement for all models over northern Africa
387 and South America relative to the case in which only orbital forcing are accounted for (MH_{PMIP}).
388 In particular, EC-Earth 3.1 and iCESM 1.2, show significant improvements in model skill as
389 benchmarked against the proxies in the MH_{GS} relative to the MH_{PMIP} experiments. On the other
390 hand, the UofT-CCSM4 and GISS-E2.1-G results show comparable scores between the MH_{GS}
391 and the MH_{PMIP} simulations. This is likely due to the fact that our calculations take into
392 consideration the improvement in proxy-model agreement concerning extent, but not the
393 magnitude of climatic changes. Notwithstanding these limitations, our work highlights the
394 importance of vegetation as key boundary condition that should be included when simulating
395 MH climate and comparing models to paleoclimate archives.

396

397 **Acknowledgments**

398 S.T. and F.S.R.P. acknowledge the financial support from the Natural Sciences and Engineering
399 Research Council of Canada (grant RGPIN-2018-04981) and the Fonds de recherche du
400 Québec–Nature et technologies (2020-NC-268559). S. T. has been partially supported by the
401 Canada Research Chairs Program (grant no. CRC 230687) and the Natural Sciences and
402 Engineering Research Council (grant no. NSERC DG 140576948). A. N. L. thanks NASA GISS

403 and NASA NCCS for institutional support. This research was supported by a National Science
404 Foundation Paleo Perspectives on Climate Change (P2C2) grant (Award #2202999) to M.L.G.

405

406 **Open Research**

407 All data presented here are accessible from the Zenodo repository:

408 <https://doi.org/10.5281/zenodo.7274836>

409 This repository contains the model outputs as well as Python scripts that can be used to reproduce
410 the figures discussed in this article.

411

412

413 **References**

414 Baker, P. A., Rigsby, C. A., Seltzer, G. O., Fritz, S. C., Lowenstein, T. K., Bacher, N. P., &
415 Veliz, C. (2001). Tropical climate changes at millennial and orbital timescales on the Bolivian
416 Altiplano. *Nature*, *409*(6821), 698-701.

417

418 Bartlein, P. J., Harrison, S. P., Brewer, S., Connor, S., Davis, B. A. S., Gajewski, K., ... & Wu,
419 H. (2011). Pollen-based continental climate reconstructions at 6 and 21 ka: a global synthesis.
420 *Climate Dynamics*, *37*(3), 775-802.

421

422 Braconnot, P., Joussaume, S., De Noblet, N., & Ramstein, G. (2000). Mid-Holocene and last
423 glacial maximum African monsoon changes as simulated within the paleoclimate modelling
424 intercomparison project. *Global and planetary change*, *26*(1-3), 51-66.

425

426 Braconnot, P., Harrison, S. P., Kageyama, M., Bartlein, P. J., Masson-Delmotte, V., Abe-Ouchi,
427 A., ... & Zhao, Y. (2012). Evaluation of climate models using palaeoclimatic data. *Nature*
428 *Climate Change*, 2(6), 417-424.

429

430 Brady, E., Stevenson, S., Bailey, D., Liu, Z., Noone, D., Nusbaumer, J., ... & Zhu, J. (2019). The
431 connected isotopic water cycle in the Community Earth System Model version 1. *Journal of*
432 *Advances in Modeling Earth Systems*, 11(8), 2547-2566.

433

434 Brierley, C., & Wainer, I. (2018). Inter-annual variability in the tropical Atlantic from the Last
435 Glacial Maximum into future climate projections simulated by CMIP5/PMIP3. *Climate of the*
436 *Past*, 14(10), 1377-1390.

437

438 Brierley, C. M., Zhao, A., Harrison, S. P., Braconnot, P., Williams, C. J., Thornalley, D. J., ... &
439 Abe-Ouchi, A. (2020). Large-scale features and evaluation of the PMIP4-CMIP6 midHolocene
440 simulations. *Climate of the Past*, 16(5), 1847-1872.

441

442 Chandan, D., & Peltier, W. R. (2020). African humid period precipitation sustained by robust
443 vegetation, soil, and Lake feedbacks. *Geophysical Research Letters*, 47(21), e2020GL088728.

444

445 Collins, J. A., Prange, M., Caley, T., Gimeno, L., Beckmann, B., Mulitza, S., ... & Schefuß, E.
446 (2017). Rapid termination of the African Humid Period triggered by northern high-latitude
447 cooling. *Nature communications*, 8(1), 1-11.

448

449 Cruz, F. W., Burns, S. J., Karmann, I., Sharp, W. D., Vuille, M., Cardoso, A. O., ... & Viana, O.
450 (2005). Insolation-driven changes in atmospheric circulation over the past 116,000 years in
451 subtropical Brazil. *Nature*, *434*(7029), 63-66.

452

453 Cruz, F. W., Vuille, M., Burns, S. J., Wang, X., Cheng, H., Werner, M., ... & Nguyen, H. (2009).
454 Orbitally driven east–west antiphasing of South American precipitation. *Nature Geoscience*,
455 *2*(3), 210-214.

456

457 Dallmeyer, A., Claussen, M., Lorenz, S. J., Sigl, M., Toohey, M., & Herzschuh, U. (2021).
458 Holocene vegetation transitions and their climatic drivers in MPI-ESM1. 2. *Climate of the Past*,
459 *17*(6), 2481-2513.

460

461 Gasse, F. (2000). Hydrological changes in the African tropics since the Last Glacial Maximum.
462 *Quaternary Science Reviews*, *19*(1-5), 189-211.

463

464 Gorenstein, I., Prado, L. F., Bianchini, P. R., Wainer, I., Griffiths, M. L., Pausata, F. S., &
465 Yokoyama, E. (2022). A fully calibrated and updated mid-Holocene climate reconstruction for
466 Eastern South America. *Quaternary Science Reviews*, *292*, 107646.

467

468 Griffiths, M. L., Johnson, K. R., Pausata, F. S., White, J. C., Henderson, G. M., Wood, C. T., ...
469 & Sekhon, N. (2020). End of Green Sahara amplified mid-to late Holocene megadroughts in
470 mainland Southeast Asia. *Nature communications*, *11*(1), 1-12.

471

472 Harrison, S. P. A., Kutzbach, J. E., Liu, Z., Bartlein, P. J., Otto-Bliesner, B., Muhs, D., ... &
473 Thompson, R. S. (2003). Mid-Holocene climates of the Americas: a dynamical response to
474 changed seasonality. *Climate Dynamics*, 20(7), 663-688.

475
476 Haug, G. H., Hughen, K. A., Sigman, D. M., Peterson, L. C., & Rohl, U. (2001). Southward
477 migration of the intertropical convergence zone through the Holocene. *Science*, 293(5533), 1304-
478 1308.

479
480 Hazeleger, W., Severijns, C., Semmler, T., Ștefănescu, S., Yang, S., Wang, X., ... & Willén, U.
481 (2010). EC-Earth: a seamless earth-system prediction approach in action. *Bulletin of the*
482 *American Meteorological Society*, 91(10), 1357-1364.

483
484 Hély, C., & Lézine, A. M. (2014). Holocene changes in African vegetation: Tradeoff between
485 climate and water availability. *Climate of the Past*, 10(2), 681-686.

486
487 Hopcroft, P. O., & Valdes, P. J. (2021). Paleoclimate-conditioning reveals a North Africa land-
488 atmosphere tipping point. *Proceedings of the National Academy of Sciences*, 118(45),
489 e2108783118.

490
491 Huo, Y., Peltier, W. R., & Chandan, D. (2021). Mid-Holocene monsoons in South and Southeast
492 Asia: dynamically downscaled simulations and the influence of the Green Sahara. *Climate of the*
493 *Past*, 17(4), 1645-1664.

494

- 495 Kageyama, M., Braconnot, P., Harrison, S. P., Haywood, A. M., Jungclaus, J. H., Otto-Bliesner,
496 B. L., ... & Zhou, T. (2018). The PMIP4 contribution to CMIP6–Part 1: Overview and over-
497 arching analysis plan. *Geoscientific Model Development*, *11*(3), 1033-1057.
- 498
- 499 Kelley, M., Schmidt, G. A., Nazarenko, L. S., Bauer, S. E., Ruedy, R., Russell, G. L., ... & Yao,
500 M. S. (2020). GISS-E2. 1: Configurations and climatology. *Journal of Advances in Modeling*
501 *Earth Systems*, *12*(8), e2019MS002025.
- 502
- 503 Levis, S., Bonan, G. B., & Bonfils, C. (2004). Soil feedback drives the mid-Holocene North
504 African monsoon northward in fully coupled CCSM2 simulations with a dynamic vegetation
505 model. *Climate Dynamics*, *23*(7), 791-802.
- 506
- 507 Lézine, A. M., Hély, C., Grenier, C., Braconnot, P., & Krinner, G. (2011). Sahara and Sahel
508 vulnerability to climate changes, lessons from Holocene hydrological data. *Quaternary Science*
509 *Reviews*, *30*(21-22), 3001-3012.
- 510
- 511 McGee, D., deMenocal, P. B., Winckler, G., Stuut, J. B. W., & Bradtmiller, L. I. (2013). The
512 magnitude, timing and abruptness of changes in North African dust deposition over the last
513 20,000 yr. *Earth and Planetary Science Letters*, *371*, 163-176.
- 514
- 515 Muschitiello, F., Zhang, Q., Sundqvist, H. S., Davies, F. J., & Renssen, H. (2015). Arctic climate
516 response to the termination of the African Humid Period. *Quaternary Science Reviews*, *125*, 91-
517 97.

518

519 Novello, V. F., Cruz, F. W., Vuille, M., Strikis, N. M., Edwards, R. L., Cheng, H., ... & Santos,
520 R. V. (2017). A high-resolution history of the South American Monsoon from Last Glacial
521 Maximum to the Holocene. *Scientific reports*, 7(1), 1-8.

522

523 Otto-Bliesner, B. L., Braconnot, P., Harrison, S. P., Lunt, D. J., Abe-Ouchi, A., Albani, S., ... &
524 Zhang, Q. (2017). The PMIP4 contribution to CMIP6–Part 2: Two interglacials, scientific
525 objective and experimental design for Holocene and Last Interglacial simulations. *Geoscientific*
526 *Model Development*, 10(11), 3979-4003.

527

528 Palchan, D., & Torfstein, A. (2019). A drop in Sahara dust fluxes records the northern limits of
529 the African Humid Period. *Nature communications*, 10(1), 1-9.

530

531 Pausata, F. S., Messori, G., & Zhang, Q. (2016). Impacts of dust reduction on the northward
532 expansion of the African monsoon during the Green Sahara period. *Earth and Planetary Science*
533 *Letters*, 434, 298-307.

534

535 Pausata, F. S., Zhang, Q., Muschitiello, F., Lu, Z., Chafik, L., Niedermeyer, E. M., ... & Liu, Z.
536 (2017). Greening of the Sahara suppressed ENSO activity during the mid-Holocene. *Nature*
537 *communications*, 8(1), 1-12.

538

539 Pausata, F. S., Emanuel, K. A., Chiacchio, M., Diro, G. T., Zhang, Q., Sushama, L., ... &
540 Donnelly, J. P. (2017). Tropical cyclone activity enhanced by Sahara greening and reduced dust

541 emissions during the African Humid Period. *Proceedings of the National Academy of Sciences*,
542 *114*(24), 6221-6226.

543

544 Pausata, F. S., Gaetani, M., Messori, G., Berg, A., de Souza, D. M., Sage, R. F., & DeMenocal,
545 P. B. (2020). The greening of the Sahara: Past changes and future implications. *One Earth*, *2*(3),
546 235-250.

547

548 Peltier, W. R., & Vettoretti, G. (2014). Dansgaard-Oeschger oscillations predicted in a
549 comprehensive model of glacial climate: A “kicked” salt oscillator in the Atlantic. *Geophysical*
550 *Research Letters*, *41*(20), 7306-7313.

551

552 Piao, J., Chen, W., Wang, L., Pausata, F. S., & Zhang, Q. (2020). Northward extension of the
553 East Asian summer monsoon during the mid-Holocene. *Global and Planetary Change*, *184*,
554 103046.

555

556 Prado, L. F., Wainer, I., & Chiessi, C. M. (2013). Mid-Holocene PMIP3/CMIP5 model results:
557 Intercomparison for the South American monsoon system. *The Holocene*, *23*(12), 1915-1920.

558

559 Rachmayani, R., Prange, M., & Schulz, M. (2015). North African vegetation–precipitation
560 feedback in early and mid-Holocene climate simulations with CCSM3-DGVM. *Climate of the*
561 *Past*, *11*(2), 175-185.

562

563 Schneider, U., Becker, A., Finger, P., Meyer-Christoffer, A., Rudolf, B., & Ziese, M. (2011).
564 GPCP full data reanalysis version 6.0 at 0.5: Monthly land-surface precipitation from rain-
565 gauges built on GTS-based and historic data. *GPCC Data Rep.*, doi, 10, 585.

566

567 Sha, L., Ait Brahim, Y., Wassenburg, J. A., Yin, J., Peros, M., Cruz, F. W., ... & Cheng, H.
568 (2019). How far north did the African monsoon fringe expand during the African humid period?
569 Insights from Southwest Moroccan speleothems. *Geophysical Research Letters*, 46(23), 14093-
570 14102.

571

572 Shanahan, T. M., McKay, N. P., Hughen, K. A., Overpeck, J. T., Otto-Bliesner, B., Heil, C. W.,
573 ... & Peck, J. (2015). The time-transgressive termination of the African Humid Period. *Nature*
574 *Geoscience*, 8(2), 140-144.

575

576 Shimizu, M. H., Sampaio, G., Venancio, I. M., & Maksic, J. (2020). Seasonal changes of the
577 South American monsoon system during the Mid-Holocene in the CMIP5 simulations. *Climate*
578 *Dynamics*, 54(5), 2697-2712.

579

580 Silva Dias, P. L., Turcq, B., Silva Dias, M. A. F., Braconnot, P., & Jorgetti, T. (2009). Mid-
581 Holocene climate of tropical South America: a model-data approach. In *Past climate variability*
582 *in South America and surrounding regions* (pp. 259-281). Springer, Dordrecht.

583

584 Sun, W., Wang, B., Zhang, Q., Pausata, F. S., Chen, D., Lu, G., ... & Liu, J. (2019). Northern
585 Hemisphere land monsoon precipitation increased by the Green Sahara during Middle Holocene.
586 *Geophysical Research Letters*, 46(16), 9870-9879.

587

588 Tabor, C., Otto-Bliesner, B., & Liu, Z. (2020). Speleothems of South American and Asian
589 monsoons influenced by a Green Sahara. *Geophysical Research Letters*, 47(22),
590 e2020GL089695.

591

592 Thompson, A. J., Tabor, C. R., Poulsen, C. J., & Skinner, C. B. (2021). Water isotopic
593 constraints on the enhancement of the mid-Holocene West African monsoon. *Earth and*
594 *Planetary Science Letters*, 554, 116677.

595

596 Tierney, J. E., Lewis, S. C., Cook, B. I., LeGrande, A. N., & Schmidt, G. A. (2011). Model,
597 proxy and isotopic perspectives on the East African Humid Period. *Earth and Planetary Science*
598 *Letters*, 307(1-2), 103-112.

599

600 Tierney, J. E., Lewis, S. C., Cook, B. I., LeGrande, A. N., & Schmidt, G. A. (2011). Model,
601 proxy and isotopic perspectives on the East African Humid Period. *Earth and Planetary Science*
602 *Letters*, 307(1-2), 103-112.

603 Wang, X., Edwards, R. L., Auler, A. S., Cheng, H., Kong, X., Wang, Y., ... & Chiang, H. W.

604 (2017). Hydroclimate changes across the Amazon lowlands over the past 45,000 years. *Nature*,

605 541(7636), 204-207.

606

607 Watrin, J., Lézine, A. M., & Hély, C. (2009). Plant migration and plant communities at the time
608 of the “green Sahara”. *Comptes Rendus Geoscience*, 341(8-9), 656-670.